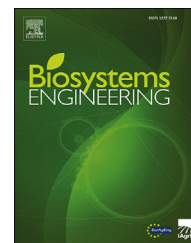


Available online at www.sciencedirect.com

ScienceDirect

journal homepage: www.elsevier.com/locate/issn/15375110

Research Paper

Numerical simulation of airflow field from a six-rotor plant protection drone using lattice Boltzmann method



Hao Zhang ^a, Lijun Qi ^{a,*}, Yalei Wu ^a, Elizabeth M. Musiu ^b,
Zhenzhen Cheng ^a, Pei Wang ^c

^a College of Engineering, China Agricultural University, Beijing, 100083, China

^b Agricultural and Biosystem Engineering Department, Jomo Kenyatta University of Agriculture and Technology, P.O. Box 62000–00200, Nairobi, Kenya

^c College of Engineering and Technology, Southwest University, Chongqing, 400715, China

ARTICLE INFO

Article history:

Received 18 March 2020

Received in revised form

21 July 2020

Accepted 26 July 2020

Published online 6 August 2020

Keywords:

Drone

Plant protection

Lattice Boltzmann

Airflow field

Numerical simulation

Rotor unmanned aerial vehicles (UAVs) for pesticide spraying have been widely used in China during the past three years. In order to improve the effectiveness of pesticide application and reduce environmental risk caused by spray drift, it is important to clarify the spatiotemporal distribution characteristics of airflow field of the drone. The airflow field produced by the UAV plays a key role in droplets delivery during the spraying. In this study, the lattice Boltzmann method (LBM) based on a mesoscopic kinetic model was used to simulate the airflow field of a six-rotor plant protection drone. The airflow field of drone in hover and at varied flight speeds ($1.0\text{--}5.0\text{ m s}^{-1}$) and various altitudes ($1.5\text{--}3.5\text{ m}$) was investigated. The characteristics of airflow separation, airflow coverage equivalent area and “steep” effect were investigated numerically. The peak value of vertical downward velocity (V_y) on the detection surface was analysed. Results indicate that the flight speed and altitude had a significant effect on the distribution of the airflow field. The predicted values in the vertical direction using the average velocity attenuation model (Y-DAVA) corresponded well with experimental measurements. The wake of airflow field had a significant backward tilt when the drone was flying forwards, thus when the flight speed was 4.0 m s^{-1} and 5.0 m s^{-1} , the wake of the airflow field lifted off the ground, whereas the transverse separation appeared as horseshoe vortices. For flight speeds of 3.0 m s^{-1} and an altitude of 3.0 m the distribution of V_y was the most uniform.

© 2020 IAGRE. Published by Elsevier Ltd. All rights reserved.

* Corresponding author.

E-mail address: qilijun@cau.edu.cn (L. Qi).

<https://doi.org/10.1016/j.biosystemseng.2020.07.018>

1537-5110/© 2020 IAGRE. Published by Elsevier Ltd. All rights reserved.

Nomenclature

UAVs	Unmanned aerial vehicles
PIV	Particle image velocimetry
WWSSN	Wireless wind speed sensor network measurement system
MDS	Molecular dynamics simulation
CFD	Computational fluid dynamics
UAH	Unmanned agricultural helicopter
DPM	Discrete phase model
RANS	Reynolds average Navier–Stokes
LBM	Lattice Boltzmann method
LBE	Lattice Boltzmann equation
BGK	Bhatnagar Gross Krook
LBGK	Lattice BGK
LES	Large eddy simulation
WALE	Wall-adapting local eddy viscosity model
Y–DAVA	Y–direction average velocity attenuation model
SSE	Sum squared residual
RMSE	Root mean squared error
R^2	R–square
\mathbf{r}	Position vector, dimensionless
f_i	Particle velocity distribution function along the i th direction
τ	Dimensionless relaxation parameter
\mathbf{e}_i	Particle velocity vectors, dimensionless
c	Ratio of lattice spacing to time step, dimensionless
f^{eq}	Equilibrium distribution function
\mathbf{u}	Fluid velocity, m s^{-1}
ρ	Density, kg m^{-3}
w_i	Weight coefficients in i th direction
ε	Constant, 10^{-6}
p	Pressure, Pa
\mathbf{a}	Acceleration, m s^{-2}
ν_T	Turbulent eddy viscosity, $\text{m}^2 \text{s}^{-1}$
$\mathbf{S}_{\alpha\beta}^d$	$\mathbf{S}_{\alpha\beta}$ Strain rate tensor of the resolved scales
$\delta_{\alpha\beta}$	Kronecker symbol
U_W	Uniform wind speed, m s^{-1}
V_F	Flight speed of drone, m s^{-1}
H_F	Flight altitude of drone, m
t	Time, s
V_{h-Yave}	Y–direction average velocity of P0–P18 on the h th horizontal section, m s^{-1}
V_{Y-pj}	Y–direction velocity of the j th sample point, m s^{-1}
h	Distance between the h th horizontal section and the XOZ plane, m
V_Y	Y–direction velocity, m s^{-1}
V_{-Y}	Vertical downward velocity, m s^{-1}
V_{+Y}	Vertical upward velocity, m s^{-1}
S	Airflow coverage equivalent area, m^2
S_0	Area of the detection surface, m^2
n	Number of sampling points
N	Total number of V_Y sampling points on the detection surface

1. Introduction

The application of pesticides is a sophisticated process with the desired result being the outcome of a complex series of biological responses (Giles, Akesson, & Yates, 2008). Aerial spray application is one of the main forms of pesticide application and has a long history (Akesson & Yates, 1974). As a component of aerial spray application equipment, the rotor-based plant protection unmanned aerial vehicles (UAVs) have developed rapidly particularly during recent years in East Asian countries such as China, South Korea and Japan (He, Bonds, Herbst, & Langenakens, 2017; Zhou et al., 2017).

Multirotor plant protection drones have achieved good results in the field due to their high efficiency and high flexibility (Lan, Chen, & Fritz, 2017; Zhang, Lan, Chen, Wang, & Liang, 2014). The advantages of multirotor plant protection drones is apparent in China, which has the largest number of small-sized farms in the world (Yang, Yang, & Mo, 2018). In addition, spraying of orchards with multirotor plant protection drones has also been reported (Jorge, Pablo, Juan, & Manuel, 2020; Tang et al., 2018; Zhang, Deng, et al., 2016). Irrespective of the crop sprayed, the rotor airflow directly determines the movement of the droplets in the air which is not only the main factor affecting droplet deposition on the target, but a major influence on spray drift (Li, Lan, & Shi, 2018). In a manner similar to the process carried out by air-assisted sprayers, the rotor airflow plays an important role in the transport droplets from their source (nozzles) to the target. Strong air jets can increase deposition by reducing droplet flight time and reducing the influence of meteorological conditions on the spray (Hong, Zhao, & Zhu, 2018). Droplets produced by the nozzles are transported to the target crop by the rotor airflow and high airflow speeds can increase the penetration of the spray into the canopy (Chen et al., 2017). High airflow speeds can cause leaves to move increasing droplet deposition on the back surfaces. However, excessive speeds may also cause damage to the crop. Different sources of airflow can lead to different spatial and temporal distribution characteristics for airflow and thus insights into the spatiotemporal distribution of airflow fields is an important prerequisite in the analysis of droplet deposition dynamics. Therefore, studies of airflow fields from multirotor drones are essential for increasing our understanding of the performance characteristics of plant protection UAVs.

In the agricultural sector two main methods have been used for studying airflow fields: field measurements using anemometers and numerical simulations with computers. In the industrial sector, the particle image velocimetry (PIV) technology has been used to measure the blade tip vortex of a single-rotor helicopter (Bauknecht, Ewers, Schneider, & Raffel, 2017; Wall & Richard, 2006) and the airflow field can also be measured using a lidar-based wind scanner (Sjöholm et al., 2014). However, it is still quite difficult to use these techniques to obtain a complete airflow fields in complex agricultural environment.

A wireless wind speed sensor network (WWSSN) was used by Wang et al. (2013) to measure the airflow field of an unmanned petrol-engined single-rotor helicopter (maximum take-off weight: 120 kg; mission payload: 25 kg) in a rice field.

Their result revealed that at constant forward speed the width of the airflow field increased with decreasing flight altitude. Li, Shi, Lan, and Guo (2019) explored the distribution of the wind field generated by the interaction between airflow of single-rotor helicopter and a rice canopy and constructed a vortex physical model. Li et al. (2015) used a WWSSN to measure the airflow field of an 18-rotor drone, and obtained a “steep” effect for the airflow field distribution parallel to the flight direction. Chen et al. (2017) measured the distribution of the airflow field of the quadrotor plant protection drone and noted that the vertical downward wind speed significantly effected deposition on the rice canopy. A characteristic of anemometer studies is that even if they include many sensors, they can only obtain wind speed data at finite locations and the three-dimensional airflow field is not fully elucidated.

Numerical simulation research is complementary to the studies in field measurement. In numerical simulation, influential factors, such as ambient wind speed and direction, atmospheric stability, and other meteorological parameters are controllable (Zhang, Tang, et al., 2016). Thus, the characteristics of the airflow field can be evaluated in isolation. Simulation methods for fluids can be divided into macroscopic, microscopic and mesoscopic method, depending on the scale of the fluid model used (Guo & Zheng, 2008). Computational fluid dynamics (CFD) method is the most mature method for predicting fluid flow. The approach solves the Navier–Stokes equation of the macroscopic continuum model (Ferziger & Perić, 2002). Zhang et al. (2015) showed that when unmanned agricultural helicopter (UAH) was used for pesticide spraying, an 8–10 m safety zone should be reserved under the condition of $1\text{--}3\text{ m s}^{-1}$ crosswinds to avoid hazards from pesticide drift. Moreover, the downwash airflow covers a circular area of approximately 3 m in radius using a 0.5 m s^{-1} boundary velocity (Zhang, Xue, Sun, Zhou, & Jin, 2017). Yang, Xue, Zhang, and Sun (2017) simulated the airflow field of the six-rotor drone (SLK-5) in hovering based on the Reynolds average Navier–Stokes (RANS) equation and found the flow characteristics of the airflow in the “inlet” and “outlet” regions of adjacent rotors caused the velocity distribution of the downwash airflow to become significantly asymmetric and the droplets were mainly distributed within the “inlet” and “outlet” regions (Yang, Xue, Cai, & Zhou, 2018). Thus, previous CFD research on the aerial spray application has been based on the three-dimensional analysis of the airflow field of multirotor drones. However, the computational accuracy of CFD is strictly dependent on the quality of the manually generated grid. Grids for the blade tip vortex and wake zone also must be manually selected which is not easy for multirotor drones with a small-scale and local geometric complexity.

The Lattice Boltzmann Method (LBM) has become an efficient approach for solving variety of difficult CFD problems (Chen, Wang, Shan, & Doolen, 1992; Janssen & Krafczyk, 2010). It has been applied accurately in many fields including hydrocyclones (Bhamjee, Connell, & Nel, 2014), micro-air vehicles (Gourdain, Jardin, Serre, Prothin, & Moschetta, 2018), helicopters (Bludau, Rauleder, Friedmann, & Hajek, 2017; Wen, Han, Lan, Yin, & Lu, 2018) and quad-rotor drones (Wen et al., 2019). This method is used to simulate the airflow field from a mesoscopic point of view. It not only avoids the

numerical dissipation problem that may be caused by manually dividing the grid, but it also has a strong dynamic adaptive refinement ability for the prediction of turbulent wakes.

The aim of the present study was to develop a three-dimensional numerical model based on the LBM to simulate the airflow field of the six-rotor plant protection drone which is currently widely used for aerial spraying in China. The aim was to study a drone in hover and at varied forward speeds ($1.0\text{--}5.0\text{ m s}^{-1}$) and at various altitudes ($1.5\text{--}3.5\text{ m}$) to provide reference data for research on the operating parameters of agricultural UAVs under coupled airflow fields. As a preliminary step, the paper focuses on the spatiotemporal distribution of the velocity field and the vorticity field, and does not consider the influence of the canopy on the airflow field. The drift and deposition of the spray and the effects of the canopy are planned for subsequent numerical simulation studies.

2. Materials and methods

2.1. Physical model of six-rotor plant protection drone

Figure 1 shows the six-rotor plant protection drone which was customised in Shenzhen JinMingRui Electronics Co., Ltd (Shenzhen City, Guangdong Province, China). The basic parameters of the drone are shown in Table 1. The drone was powered by an external power supply and the rotor rotational speed was regulated by a wireless remote controller. In addition, a non-contact tachometer (Jintan Runchen Electric Appliance Factory, Changzhou City, Jiangsu Province, China) was installed to monitor rotor rotational speed. To ensure measurement accuracy, the horizontal mounting distance of the Hall element to the magnet fixed on the brushless motor was $< 5.0\text{ mm}$. Screw bolts were used to secure the drone to the bracket in the laboratory (Plant Protection Machinery Laboratory, China Agricultural University, China).

2.2. Simplified model used in numerical simulation

The rotor is an important part of the drone, which produces both the airflow field and the necessary lift for the drone. In this study, an automatic three-dimensional optical scanning system (CaMega MCS-5/4-axis, BoWeiHengXin, China) was used to reconstruct the rotors of clockwise rotation and anticlockwise rotation, respectively. Thus, an accurate three-dimensional model of the rotor was obtained (Fig. 2).

In order to save on computer resources, the physical model of the drone was rationally simplified according to the previous research (Guo et al., 2020; Yang, Xue, et al., 2018; Yang et al., 2017; Zhang et al., 2019) with only the rotor was considered in the numerical simulation. Simplifying the method has been found to have little effect on the development and evolution of airflow (Yang et al., 2017). Figure 3 shows the simplified model for simulation. The rotors 1, 3, and 5 were designed to rotate in an anticlockwise direction, whereas the rotors 2, 4, and 6 rotated in a clockwise direction. A Cartesian coordinate system in space was defined, where the negative directions of the X and Y axes were respectively,

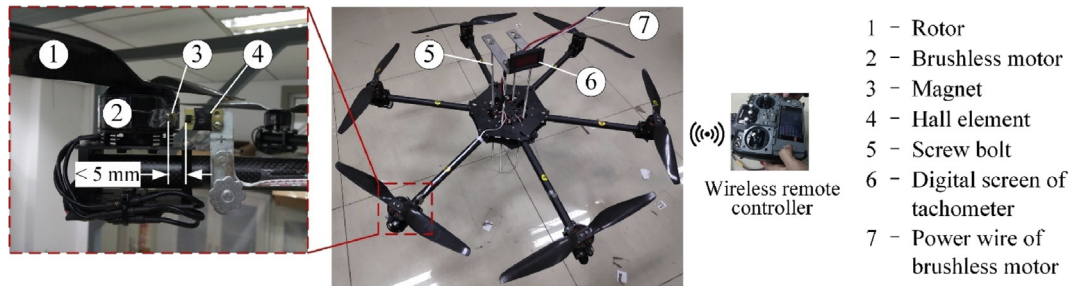


Fig. 1 – Six-rotor plant protection drone.

Table 1 – Basic parameters of the six-rotor plant protection drone.

Parameter description	Value	Parameter description	Value
Wheelbase	0.8 m	Number of rotors	6
Rotor diameter	0.381 m	Brushless motor	X4114 KV370
Rotor pitch	0.1397 m	Maximum drug loading	5 kg

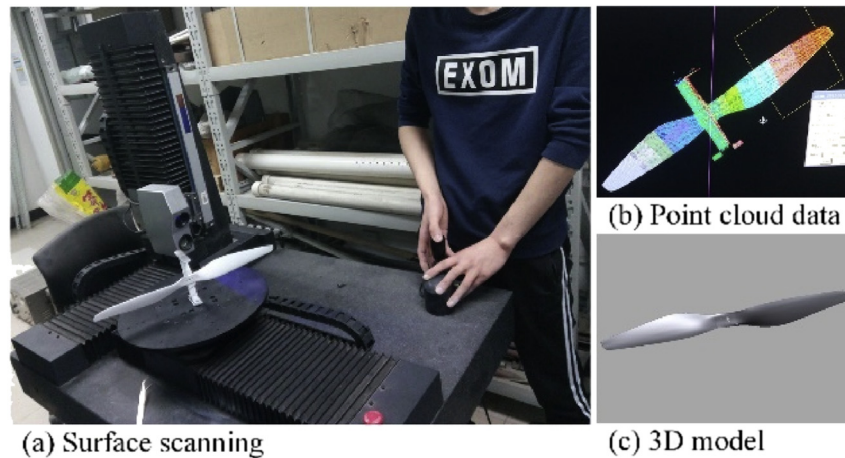


Fig. 2 – Rotor reverse modelling.

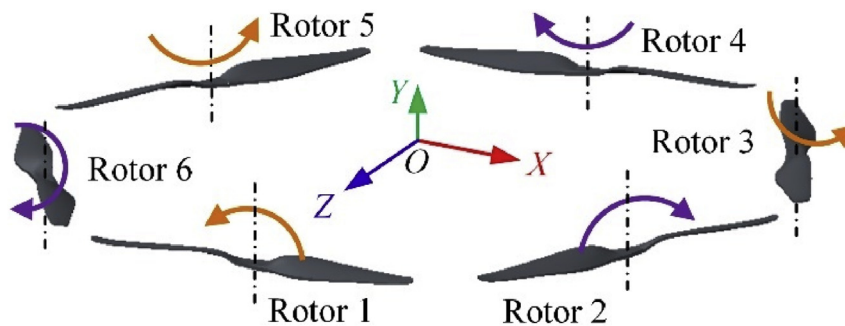


Fig. 3 – Simplified model of six-rotor plant protection drone.

the forward and vertical directions of the drone and the Z axis was across the plane of the rotors. The origin of the coordinate system is located at the centre of the six rotors on the plane. Thus, the XOZ plane coincided with the plane formed by the six rotors.

2.3. Numerical simulation approach

The three-dimensional simulations of airflow field of the drone were conducted using Xflow 2017x software (Dassault Systèmes, Paris, France) in hovering and at varied flight

speeds and altitudes conditions. The simulations were carried out using Dell XPS 8930 with Intel Core i7–8700 (6 cores, 12 threads, 3.2 GHz, 16 GB RAM).

2.3.1. Lattice Boltzmann method

The Lattice Boltzmann equation (LBE) model consists of three elements: the discrete velocity set of fluid particles, the lattice structure and the evolution equation (Guo & Zheng, 2008). This equation describes the motion of a fluid particle distribution function with discrete velocities over a lattice (Malaspinas & Sagaut, 2014). In this paper, the lattice structure was D3Q27 (Fig. 4). Each discrete node had 27 discrete velocity vectors, which can better describe the three-dimensional motion behaviour of fluids (Premnath & Banerjee, 2011).

The calculations associated with the particle collision term in the original nonlinear LB equation require excessive storage and computational cost; however, for most practical cases, the collision term can be simplified to the single relaxation time Bhatnagar Gross Krook (BGK) collision operator (Aidun & Clausen, 2010). The obtained LB equation with a single relaxation time, called the LBGK equation, can effectively reduce computational cost. The evolution equation was described by Aidun and Clausen (2010):

$$f_i(\mathbf{r} + \mathbf{e}_i, t + 1) - f_i(\mathbf{r}, t) = -\frac{1}{\tau} (f_i(\mathbf{r}, t) - f_i^{\text{eq}}(\mathbf{r}, t)) \quad (1)$$

where \mathbf{r} is position vector; t is the time; s ; f_i is the particle velocity distribution function along the i th direction. τ is the dimensionless relaxation parameter.

The particle velocity vectors \mathbf{e}_i for a D3Q27 lattice model were defined according to Premnath and Banerjee (2011) as:

$$\mathbf{e}_i = \begin{cases} (0, 0, 0)c, & i = 0 \\ (\pm 1, 0, 0)c, (0, \pm 1, 0)c, (0, 0, \pm 1)c, & i = 1, \dots, 6 \\ (\pm 1, \pm 1, 0)c, (\pm 1, 0, \pm 1)c, (0, \pm 1, \pm 1)c, & i = 7, \dots, 18 \\ (\pm 1, \pm 1, \pm 1)c, & i = 19, \dots, 26 \end{cases} \quad (2)$$

where c is the ratio of lattice spacing to time step, $c = 1$.

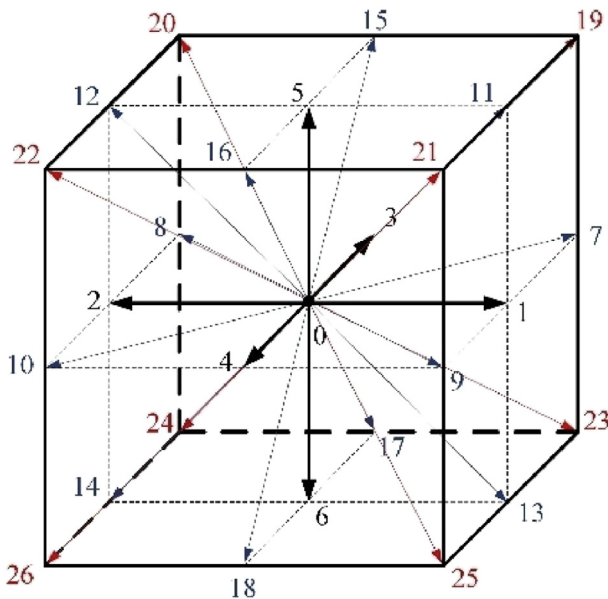


Fig. 4 – Schematic diagram of D3Q27 lattice.

By using the Taylor series expansion of the Maxwell–Boltzmann distribution function with fluid velocity \mathbf{u} up to second order, the equilibrium distribution function f_i^{eq} is obtained as (Chen & Doolen, 1998; Qiu, Tian, Liu, & Han, 2019):

$$f_i^{\text{eq}} = \rho w_i \left[1 + \frac{\mathbf{e}_i \cdot \mathbf{u}}{c_s^2} + \frac{(\mathbf{e}_i \cdot \mathbf{u})^2 - (c_s |\mathbf{u}|)^2}{2c_s^4} \right] \quad (3)$$

where constant sound speed $c_s = c/\sqrt{3}$ and the weight coefficients are written as

$$w_i = \begin{cases} 8/27 & i = 0 \\ 2/27 & i = 1, \dots, 6 \\ 1/54 & i = 7, \dots, 18 \\ 1/216 & i = 19, \dots, 26 \end{cases} \quad (4)$$

The macroscopic density ρ (kg m^{-3}), velocity \mathbf{u} (m s^{-1}) and pressure p (Pa) were computed as:

$$\rho = \sum_{i=0}^{26} f_i \quad (5)$$

$$\mathbf{u} = \sum_{i=0}^{26} \mathbf{e}_i f_i + \frac{1}{2} \mathbf{a} t \quad (6)$$

where \mathbf{a} is the acceleration, m s^{-2} .

$$p = \rho c_s^2 \quad (7)$$

2.3.2. Turbulence model

Turbulence was modelled using large eddy simulation (LES). This scheme introduces an additional viscosity, called turbulent eddy viscosity ν_T , in order to model the sub-grid turbulence (Weickert, Teike, Schmidt, & Sommerfeld, 2010). The LES scheme applied was the wall-adapting local eddy viscosity model (WALE). The implementation was formulated as:

$$\nu_T = (C_W \Delta)^2 \frac{(\mathbf{S}_{\alpha\beta}^d \mathbf{S}_{\alpha\beta}^d)^{\frac{3}{2}}}{(\mathbf{S}_{\alpha\beta}^d \mathbf{S}_{\alpha\beta}^d)^{\frac{5}{2}} + (\mathbf{S}_{\alpha\beta}^d \mathbf{S}_{\alpha\beta}^d)^{\frac{5}{4}} + \epsilon} \quad (8)$$

in which

$$\mathbf{S}_{\alpha\beta}^d = \frac{1}{2} (\mathbf{g}_{\alpha\beta}^2 + \mathbf{g}_{\beta\alpha}^2) - \frac{1}{3} \delta_{\alpha\beta} \mathbf{g}_{\gamma\gamma}^2 \quad (9)$$

$$\mathbf{S}_{\alpha\beta} = \frac{\mathbf{g}_{\alpha\beta} + \mathbf{g}_{\beta\alpha}}{2} \quad (10)$$

where ν_T is the turbulent eddy viscosity, $\text{m}^2 \text{s}^{-1}$; the constant C_W is typically 0.325; Δ is the characteristic length scale representing the cell size, and $\epsilon = 10^{-6}$; $\mathbf{S}_{\alpha\beta}^d$, $\mathbf{S}_{\alpha\beta}$ is the strain rate tensor of the resolved scales and $\delta_{\alpha\beta}$ is the Kronecker symbol.

2.3.3. Computational domain

The computational domain was set up as a virtual wind tunnel forming a cuboid with length \times width \times height in X, Z and Y directions, respectively. The dimensions were shown in Table 2. The simplified model of drone (Fig. 3) was placed inside the virtual wind tunnel as shown in Fig. 5 and different flight speeds of the drone were simulated by setting different wind speeds at the inlet of the virtual wind tunnel. The wind direction was from $-X$ to $+X$.

Table 2 – Flight parameters of the studied drone, size of the computational domain and the lattice number.

Case	Flight speed $V_F=Uw$ (m s ⁻¹)	Flight altitude H_F (m)	Computational domain (m)			Lattice number	
			(-X, +X)	(-Y, +Y)	(-Z, +Z)	t = 0 s	t = 2.5 s
1 (validation)	0 (in hover)	2.5	(-4, +4)	(-2.5, +1.5)	(-4, +4)	271,274	16,885,151
2	0 (in hover)	3.0	(-4, +4)	(-3, +2)		552,610	19,609,109
3	1.0	3.0	(-3, +5)	(-3, +2)		280,212	17,301,237
4	2.0	3.0	(-2, +6)	(-3, +2)		280,212	22,179,656
5	3.0	3.0	(-2, +10)	(-3, +2)		300,212	23,470,485
6	4.0	3.0	(-2, +10)	(-3, +2)		300,212	24,530,261
7	5.0	3.0	(-2, +10)	(-3, +2)		300,212	25,344,091
8	2.0	1.5	(-2, +6)	(-1.5, +1.5)		275,274	15,255,561
9	2.0	2.0	(-2, +6)	(-2, +2)		272,212	20,003,602
10	2.0	2.5	(-2, +6)	(-2.5, +1.5)		271,274	20,879,617
11	2.0	3.5	(-2, +6)	(-3.5, +1.5)		279,274	22,950,839

2.3.4. Boundary conditions

Boundary conditions were specified to simulate the virtual wind tunnel (Men, Lai, Dong, Du, & Liu, 2017). The faces of the computational domain were defined as *Inlet*, *Outlet*, *Left*, *Right*, *Top*, *Ground* and *UAV* as show in Fig. 5. A uniform wind speed (Uw) entered the computational domain from the *Inlet*. The *Left* and *Right* side of the cuboid were assigned the periodic boundary conditions. The bottom face (*Ground*) was assigned wall boundary conditions with enhanced wall-function. The inlet boundary condition with zero velocity profile and zero of gauge pressure was applied at the *Top*. No-slip, adiabatic and inert wall boundary conditions were applied at the rotor surface of drone. Single phase model with air was applied to investigate the airflow field. A total of eleven cases considering flight parameters (speed and altitude) as well as hover were selected to study the distribution characteristics of airflow field. Initial conditions are listed in Table 2.

2.3.5. Spatial discretisation

Xflow is a meshless based particle solution that eliminates the time-consuming process of manual meshing (Men et al., 2017). In the pre-treatment process, an initial octree lattice structure was generated according to user-specified resolution for each geometry. The finer the spatial discretisation of the domain the more accurate the solution but the more elements to be computed (Men et al., 2017). As shown in Table 3, a spatial resolution of 0.2 m was used in the far field (the lowest

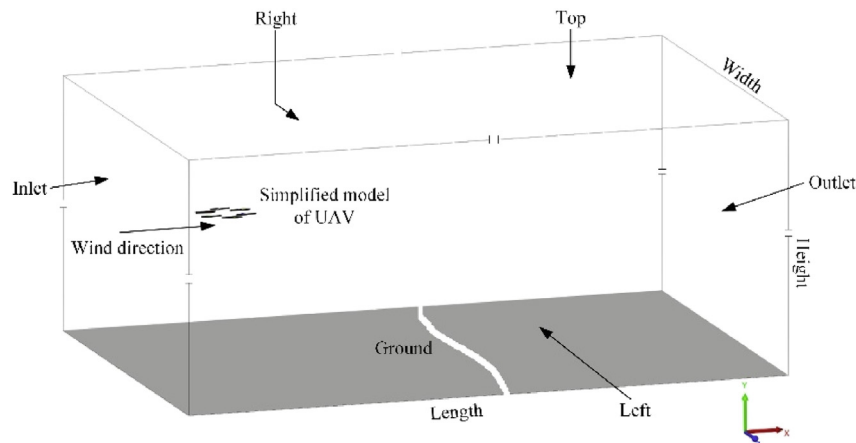
Table 3 – Lattice resolutions and wake refinement threshold with the adaptive wake refinement strategy.

ID	Surfaces or regions	Resolution or threshold
1	Far field	0.2 m
2	Rotor surfaces	0.00625 m
3	Wake refinement	0.0125 m
4	Wake refinement threshold	1e-05 s ⁻¹

resolution) but in the regions close to the rotor surface, a very fine lattice resolution of 0.00625 m was used. A wake refinement size of 0.0125 m and a threshold of 1e-05 s⁻¹ was chosen for the simulation, which allowed a relatively low lattice number but with acceptable results. The dynamic wake refinement algorithm was applied, which can dynamically refine the wake generated. As shown in Table 2, the lattice number increased during the simulation process. Figure 6 shows the spatial discretisation result of the wake of case 1 after 2.5 s. Also, when $t = 2.5$ s, the airflow in the computational domain had fully dispersed in all of the cases studied and this value was used for the simulation time.

3. Numerical approach to validation

The instantaneous velocity field in the forward-flight application could not be determined because of experimental

**Fig. 5 – Schematic diagram of computational domain.**

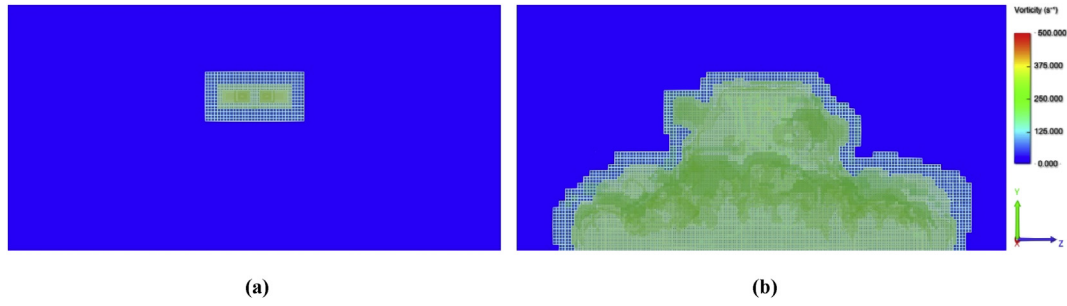


Fig. 6 – The lattice distribution using adaptive wake refinement strategy of case 1. (a) 271,274 elements at time = 0 s; (b) 16,885,151 elements at time = 2.5 s.

limitations. Case 1 was used as a substitute for the forward-flight cases to evaluate the accuracy of the simulation model. Firstly, a Y-direction average velocity attenuation (Y-DAVA) model was established using case 1 simulated data. Measured values were compared with the predicted values of the Y-DAVA model. Then, the distribution characteristics of the airflow field for the other cases were compared with the results obtained by Li et al. (2014, 2015).

3.1. Data acquisition and processing method

For the simulation results of case 1, a horizontal section was selected at every 0.01 m on the Y axis (from $Y = -0.2$ m to $Y = -2.5$ m), and the nineteen sample points distributed on each horizontal section (P0 – P18). As shown in Fig. 7a, P0 was on the Y axis, P1 – P6 and P7 – P18 were evenly distributed on circles of radius 0.2 m and 0.4 m, respectively while P7, P9, P11, P13, P15, and P17 were located directly below the rotor 1, 2, 3, 4, 5 and 6, respectively. The Y-direction average velocity of P0 – P18 on each horizontal section was obtained using Eq. (11). With h as the abscissa and V_{h-Yave} as the ordinate, a polynomial fit was performed to establish the Y-DAVA model.

$$V_{h-Yave} = \sum_{j=0}^n V_{Y-Pj} / n \quad (11)$$

where V_{h-Yave} is the Y-direction average velocity of P0 – P18 on the h th horizontal section, $m\ s^{-1}$; V_{Y-Pj} is the Y-direction velocity of the j th sample point, $m\ s^{-1}$; $h = |Y|$ represents the distance between the h th horizontal section and the XOZ plane, m; n is the number of sampling points, 19.

Four horizontal sections ($h = 0.5$ m, 1.0 m, 1.5 m and 2.0 m) were taken and the airflow velocity of P0 – P18 on the four horizontal sections measured using a hot wire anemometer (Testo 405i, Titisee-Neustadt, Germany) (Fig. 7b). The anemometer recorded data at every 2 s and transmitted it via Bluetooth to an application on a smart phone. The measurement time for each sample point was 40 s, and the calculated average velocity was recorded as V_{Y-Pj} (Yang et al., 2017).

3.2. Results and validation

As shown in Table 4, an increase in polynomial fitting order gradually decreased the sum squared residual (SSE) and the also the root mean squared error (RMSE) but it increased the R-square (R^2). The closer the SSE and the RMSE were to zero, the closer the R^2 was to 1 and the more accurate was the Y-DAVA model (Li et al., 2015). At orders greater than the 6th order, the values for SSE, RMSE and R^2 tended to stabilise. Therefore, a 6th order polynomial fitting result was selected since it had low complexity whilst ensuring accuracy. The model formula and coefficients are shown in Eq. (12) and Table 5, respectively.

Moreover, all measurements ($V_{0.5-Yave} = 5.62\ m\ s^{-1}$, $V_{1.0-Yave} = 4.46\ m\ s^{-1}$, $V_{1.5-Yave} = 4.14\ m\ s^{-1}$ and $V_{2.0-Yave} = 3.16\ m\ s^{-1}$) were within 95% prediction interval of the Y-DAVA model (Fig. 8). It was clear that the results not only confirmed accuracy of the Y-DAVA model, but also affirmed the reliability of the simulated results. The trend of V_{h-Yave} was divided into five zones: zone I (<0.375 m), zone II (0.375 m–0.75 m), zone III (0.75 m–1.5 m), zone IV

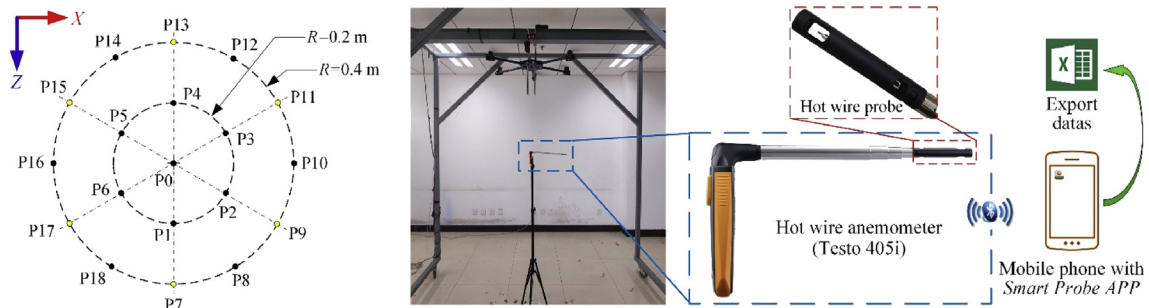


Fig. 7 – The Y-direction velocity test experiment. (a) Schematic diagram of the distribution of sample points; (b) The Y-direction velocity test experiment.

Table 4 – Polynomial fitting parameter value statistics.

$$V_{h-Yave} = \text{Intercept} + B_1h + B_2h^2 + B_3h^3 + B_4h^4 + B_5h^5 + B_6h^6 \quad (12)$$

Order	SSE	RMSE	R ²
2	45.48457	0.44862	0.85419
3	19.8252	0.29684	0.93645
4	15.8309	0.26585	0.94925
5	13.67187	0.24761	0.95617
6	5.09363	0.15147	0.98367
7	4.60703	0.14438	0.98523
8	4.5594	0.14396	0.98538
9	3.68095	0.12965	0.98820

(1.5 m–2.25 m) and zone V (>2.25 m). In zone I, the V_{h-Yave} values increased gradually to nearly 6 m s^{−1} but attenuated in zones II, IV and V. It was noted that the attenuation rates in zones II and IV was the same but were higher in zone V, finally decayed to 0 m s^{−1}. This was probably because zone V was close to the ground (Yang et al., 2017). The V_{h-Yave} value in zone III was relatively stable at around 4.5 m s^{−1}. This agreed with previous observations by Zhang et al. (2019) who noted a “speed stability zone” in the vertical direction. Although the rotor airflow field had transient characteristics, the Y–DAVA model was still useful in highlighting the average characteristics of airflow velocity changes in the vertical direction as well as the possible effects on spray delivery.

4. Results and discussions

4.1. Airflow field in hovering

Figure 9 shows the spatiotemporal distribution of the airflow field vorticity for case 2. When $t = 1.0$ s (Fig. 9a), the downwash airflow reached the ground, but did not spread on the ground. The shape of the airflow appeared nearly “cylindrical”, similar to the observation made by Zhang et al. (2019). For $t = 1.5$ s (Fig. 9b), the downwash airflow was blocked by the ground and diffused along the ground surface to form a ground spreading airflow. A vortex ring appeared at the limits of the ground spreading airflow. When $t = 2.5$ s (Fig. 9c), the ground spreading airflow no longer diffused in an outward direction but rather formed a stable vortex ring structure. This implied that the airflow in the computational domain had fully

dispersed. In their work, Wen et al. (2019) did not reveal ground spreading of airflow or a vortex ring.

As shown in Fig. 9d, the evolution of the downwash airflow produced a spiral wake vortex, turbulent wake, ground a spreading airflow, and a vortex ring. In addition, partially dissipated escape vortices occurred at the boundary of the airflow field during the evolution process. As with a single-rotor aircraft (Wen et al., 2018), wingtip vortices occurred at the tips of the six-rotors, and vortex cores were located at the wingtips (Fig. 9e). However, due to the small distance between the rotors, there was a significant interference at the wingtip vortex (inter-wing interference). Induced by the wingtip vortex, a spiral wake vortex appeared within 0 m–0.5 m below the drone, and radial contraction occurs (Fig. 9d). As the airflow developed downward, the six spiral wake vortices approached each other so that serious interference occurred. This destroyed the spiral wake vortex structure, causing it to lose its coherence diffuse into a turbulent wake. The turbulent wake region was the main distribution area of the droplets in the downwash airflow field, and played a major role in the delivery of the droplets. The airflow distribution range in this area determined the spatial distribution range of the droplets, and the airflow velocity determined the motion state of the droplets (Li et al., 2018). In addition, at the boundary of the airflow field in the turbulence wake region, the escape vortex may have carried small droplets horizontally, causing them to drift and eventually be deposited in non-target areas.

In order to demonstrate the time-varying characteristics of downwash airflow, Fig. 10 shows the evolution of the V_{h-Yave} with time for case 2; $h = 0.5$ m, 1.0 m, 1.5 m, 2.0 m and 2.5 m, respectively. From 0 to 0.5 s, for $h = 0.5$ m, 1.0 m and 1.5 m, V_{h-Yave} increased rapidly; for $h = 2.0$ m and 2.5 m, it increased slowly. From 0.5 to 1.0 s, for $h = 2.0$ m and 2.5 m, V_{h-Yave} increased rapidly. This agreed with the principle of a top-down development of airflow being simulated. At 0.5 s, the V_{h-Yave} of $h = 0.5$ m was smaller than that of $h = 1.0$ m. This was because the downwash airflow at $h = 0.5$ m was mainly spiral wake vortex and its distribution was relatively concentrated, resulting in the velocity values of some sampling points being smaller. Another important reason was that the airflow was unstable from 0 to 1.0 s for $h = 1.0$ m. From 1.0 to 1.5 s, the V_{h-Yave} decreased for $h = 2.0$ m and 2.5 m, which was caused by the ground effect (Yang et al., 2017). In addition, for $h = 0.5$ m and 1.0 m, the V_{h-Yave} became stable at 0.5 s and 1.0 s respectively; for $h = 1.5$ m, 2.0 m and 2.5 m, the V_{h-Yave} became stable at 1.5 s. However, the V_{h-Yave} still had small fluctuation, caused by turbulence due to the high rotational speed of the rotors. Combined with the analysis of Fig. 9b,c, although the V_{h-Yave} became stable at 1.5 s, it only showed that the airflow in the Y-direction was fully developed, and that the ground spreading airflow continued to diffuse outward.

4.2. Wake characteristics at different flight speeds

In order to investigate the influence of drone flight speed on wake characteristics, different flight speeds at a constant flight altitude were simulated (case 3 to case 7). Figure 11 shows the vorticity distribution of the airflow field at different flight speeds (1 m s^{−1} to 5 m s^{−1}) when $t = 2.5$ s and $H_F = 3.0$ m. Compared with the airflow field of drone in

Table 5 – Six-order polynomial fitting coefficient statistics.

Fitting coefficient	Coefficient value	95% confidence interval
Intercept	−3.16343	(−3.9849, −2.34196)
B ₁	63.47499	(57.6675, 69.28249)
B ₂	−166.61572	(−181.56101, −151.67041)
B ₃	200.17993	(181.81628, 218.54358)
B ₄	−122.0744	(−133.67436, −110.47444)
B ₅	36.79174	(33.16163, 40.42184)
B ₆	−4.36863	(−4.81388, −3.92338)

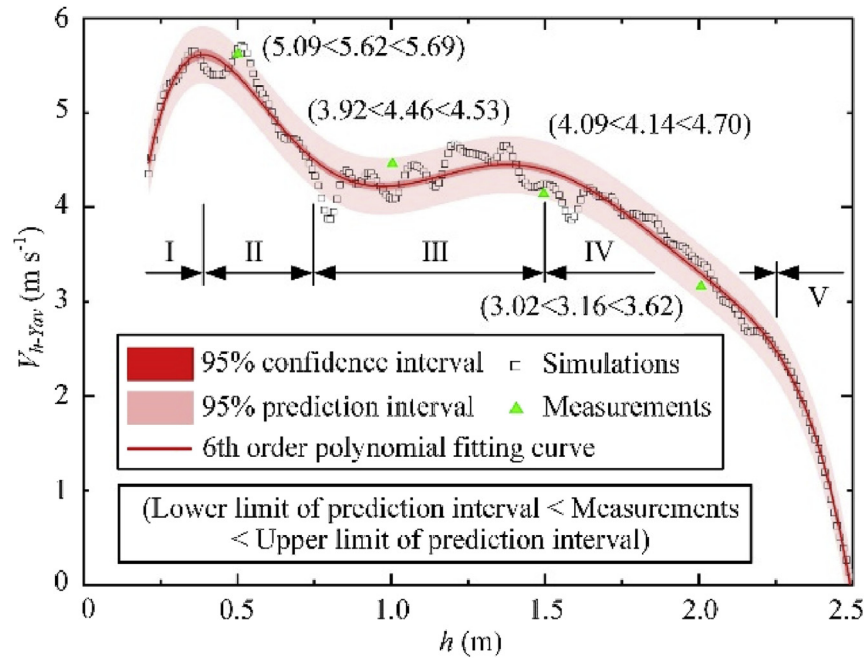


Fig. 8 – Comparison of anemometer measurements and predicted values of Y-DAVA model.

hovering, the wake of airflow field had a significant backward tilt when the drone was flying forward. This will cause the deposition position of the droplets to move to the rear of the drone. As shown in Fig. 11, the greater the flight speed of the drone, the more the wake of the airflow field was tilted backward. The wake was axisymmetric (Y-axis) for all cases.

When $V_F = 1.0 \text{ m s}^{-1}$ (Fig. 11a–c), the wake of the airflow field was tilted less towards the rear of the drone and had a ground spreading airflow and vortex ring. The ground spreading airflow spread further behind the drone, causing

the centre of the vortex ring to move towards the rear of the drone by a distance of 2.0 m (Fig. 11b). When $V_F = 2.0 \text{ m s}^{-1}$ (Fig. 11d–f), the extent to which the wake tilted toward the rear of the drone increased. Although the airflow reached the ground at 2.0 m behind the drone, the vortex ring disappeared, and the ground spreading airflow completely spread to the rear of the drone. The wake also had airflow separation, including in the vertical Y-direction (Fig. 11e) and transverse (right and left, Z-direction) (Fig. 11f) separation of airflow. The transverse separation airflow was “Λ-shaped” and

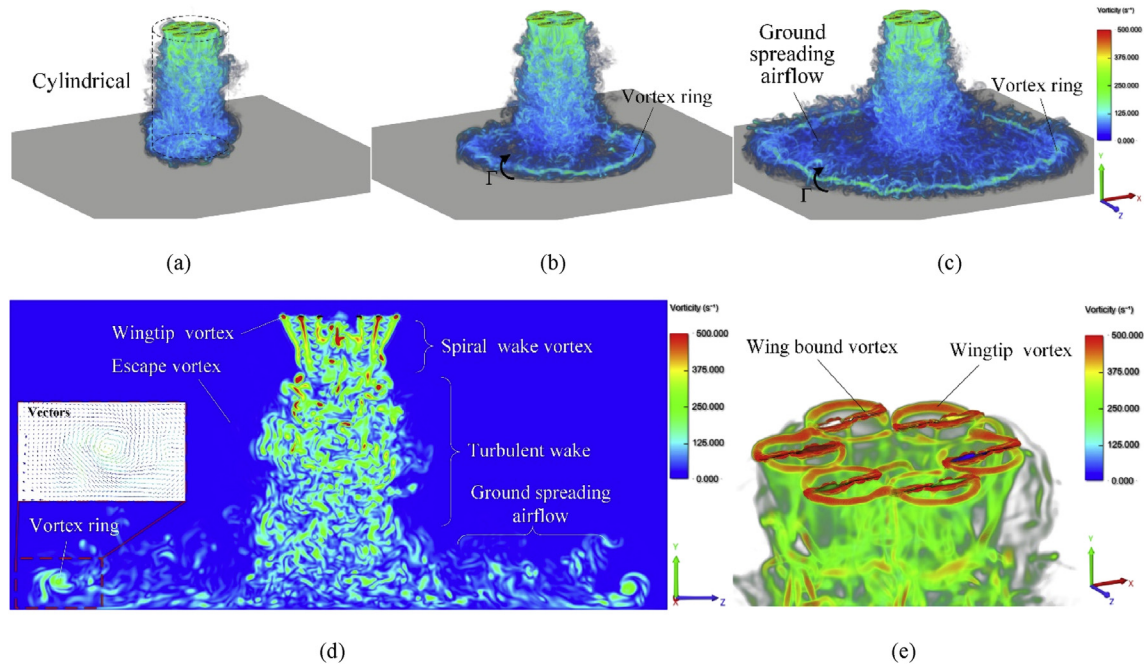


Fig. 9 – Vorticity spatiotemporal distribution diagram of airflow field ($H_F = 3.0 \text{ m}$). (a) $t = 1.0 \text{ s}$. (b) $t = 1.5 \text{ s}$. (c) $t = 2.5 \text{ s}$. (d) Vorticity distribution diagram in YOZ plane ($t = 2.5 \text{ s}$). (e) Wing-tip vortex diagram ($t = 2.5 \text{ s}$).

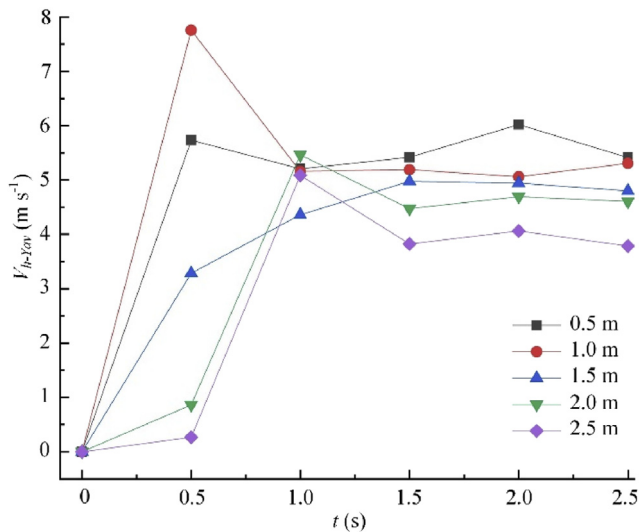


Fig. 10 – Y-direction average velocity at different times for case 2.

symmetrical. Li et al. (2014) carried out field measurements on the airflow field of a multirotor drone, and found two velocity peaks central to the airflow in the horizontal direction which corresponded to the separation of the airflow in the transverse direction seen in this work. The vertical downwards separation of airflow may help deliver sprays directly towards the target but upwards separation of the airflow may entrain fine droplets lengthening the time the spray remains airborne increasing the risk of drift and evaporation. Transverse separation may increase the width of the airflow field and although it may help rice pollination (Li et al., 2014) it can displace pesticide spray causing uneven deposition of droplets in the transverse direction. When $V_F = 3.0 \text{ m s}^{-1}$ (Fig. 11g–i), the inclination of the wake towards the rear of drone continued to increase and the width of the airflow field decreased causing no airflow separation. The airflow reached the ground at 5.0 m behind the drone (Fig. 11h).

When $V_F = 4.0 \text{ m s}^{-1}$ (Fig. 11j–l) and $V_F = 5.0 \text{ m s}^{-1}$ (Fig. 11m–o), the wake was detached from the ground and the distribution of the airflow field in the vertical direction became narrow. The wake extended obliquely towards the rear of the drone to 9.0 m when $V_F = 4 \text{ m s}^{-1}$ (Fig. 11k) but still showed a "Λ-shape" symmetrical in the transverse direction (Fig. 11l). Moreover, as the flight speed increased to 4.0 m s^{-1} and 5.0 m s^{-1} , the transverse separation of the wake appeared as two horseshoe vortices similar to those described by Wen et al. (2019). At this time, the wake was not strong enough to deliver droplets to the target directly although droplets may eventually settle on the surface of crop canopy by gravity and atmospheric turbulence. This process can not only affect the deposition of spray inside the crop canopy, but also increase the risk of spray drift occurring behind the drone. Therefore, when the flight speed was at 4.0 m s^{-1} and 5.0 m s^{-1} , it appears that our research indicates that conditions are no longer suitable for pesticide application.

The horseshoe vortex extended obliquely to the rear of the drone for a distance of 2.0 m when $V_F = 5.0 \text{ m s}^{-1}$ and then the horseshoe vortex gradually climbed to the drone's flying

height, extending backwards maintaining the same height. The final extension distance of the wake exceeded 10.0 m (Fig. 11n). In the transverse direction, the horseshoe vortex firstly spread out to both sides and then shrunk as it extended to the rear of the drone (Fig. 11o).

When the drone was flying at a low speed (i.e. 1.0 m s^{-1}) (Fig. 11a), the wake was similar to that found in hovering as no horseshoe vortex was observed. However, as the flight speed increased to 2.0 m s^{-1} and 3.0 m s^{-1} (Fig. 11d,g), the shape of the horseshoe vortices on both sides of the airflow field gradually became more apparent. When the flight speed of the drone was increased to 4.0 m s^{-1} and 5.0 m s^{-1} (Fig. 11j,m), the wake was completely in the shape of horseshoe vortices. It is worth noting that the non-horseshoe wake was found along the axis of symmetry (Y-axis) in Fig. 11m. This phenomenon may be related to the rotor layout of the drone (i.e. either "×" type or "+" type in the forward flight direction).

4.3. Wake characteristics at different flight altitudes

In order to investigate the influence of drone flight altitude on wake characteristics, different flight altitudes at a constant flight speed were simulated (case 8 to case 11 and case 4). Figure 12 shows the vorticity distribution of the airflow field at different flight altitudes (1.5 m–3.5 m) when $t = 2.5 \text{ s}$ and $V_F = 2.0 \text{ m s}^{-1}$. Similarly, the wake was axisymmetric (Y-axis) for all cases.

Figures 12b,e,h,k and n illustrates that when the flight speed of drone was maintained constant at 2 m s^{-1} , as the flight altitude increased, the vertical separation of the airflow field became gradually apparent. By contrast, the transverse separation of the airflow field gradually weakened (Fig. 12c,f,i,l and o). The cause of this phenomenon may be that because the drone was flying at a low altitude (1.5 m and 2.0 m), the space extended by the horseshoe vortices on both sides of the airflow field was limited in the vertical direction (Fig. 12a,d). The airflow field had reached the ground before vertical separation occurred. When the flight altitude increased to 2.5 m, 3 m, and 3.5 m (Fig. 12g,j and m), the horseshoe vortices on both sides of the airflow field became fully developed extending to the rear of the drone and dissipating. The formation and development of horseshoe vortices on both sides of the airflow field are the main reasons for the vertical separation of airflow.

Also, when the flight altitude was 1.5 m or 2.0 m (Fig. 12c,f), the downwash airflow reached the ground at a relatively large velocity, and due to the ground effect and the transverse separation of the airflow was greater. The width of the airflow field reached 6.0 m (Fig. 12a,d). When the flight altitude increased to 2.5 m, 3.0 m, and 3.5 m (Fig. 12i,l and o), the downwash airflow reached the ground at a relatively low velocity, and the ground effect gradually weakened, causing the transverse separation of the airflow to gradually decrease. The width of the airflow field reached 5.0 m, 4.0 m and 3.0 m, respectively (Fig. 12g,j and m). As the flight altitude increased, the width of the airflow field gradually decreased. The main reason being that ground effect decreases with increasing flight altitude causing the transverse spread of the airflow to decreased. Moreover, the horseshoe vortices on both sides of the airflow field contracted toward the centre as flight altitude increased.

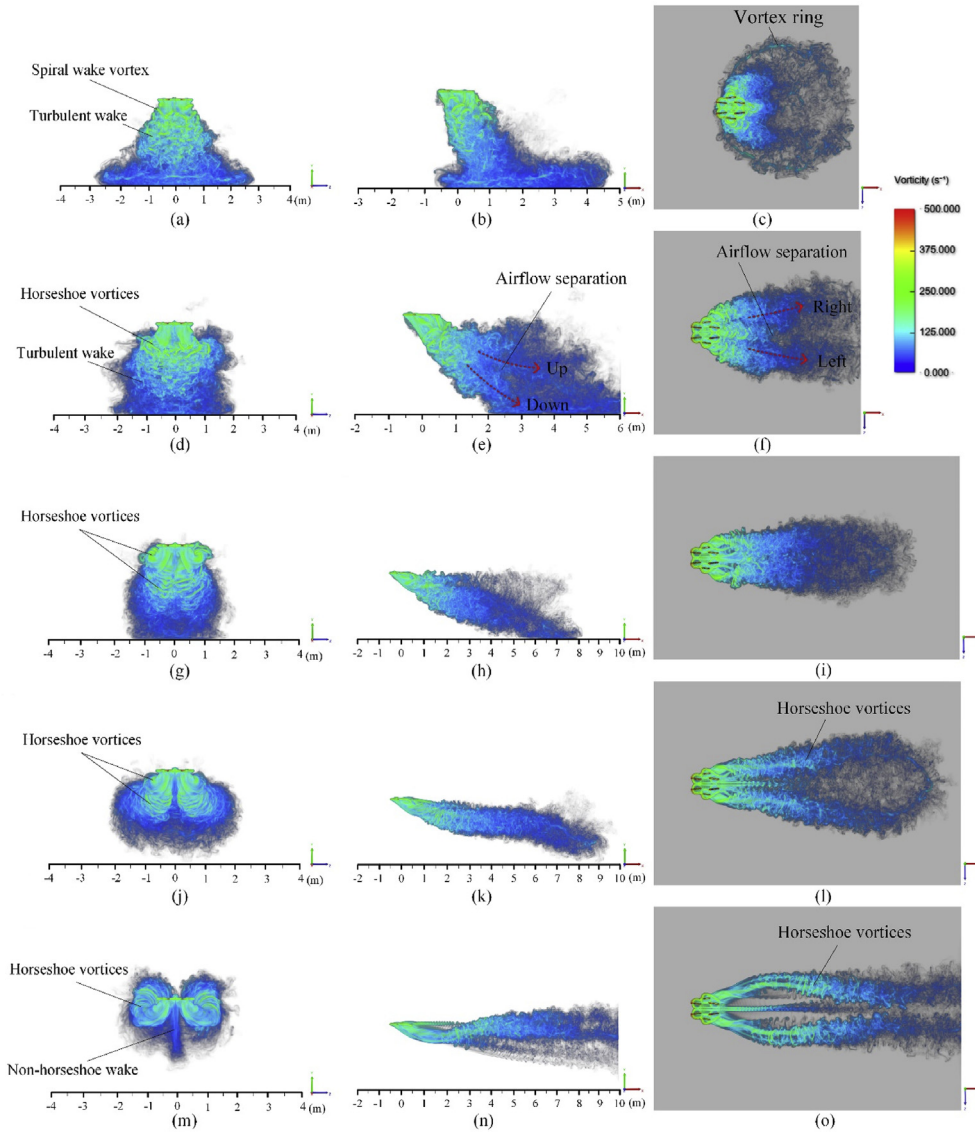


Fig. 11 – Vorticity distribution diagram at different flight speeds ($H_F = 3.0$ m, $t = 2.5$ s). (a) $V_F = 1.0$ m s⁻¹, front view. (b) $V_F = 1.0$ m s⁻¹, lateral view. (c) $V_F = 1.0$ m s⁻¹, top view. (d) $V_F = 2.0$ m s⁻¹, front view. (e) $V_F = 2.0$ m s⁻¹, lateral view. (f) $V_F = 2.0$ m s⁻¹, top view. (g) $V_F = 3.0$ m s⁻¹, front view. (h) $V_F = 3.0$ m s⁻¹, lateral view. (i) $V_F = 3.0$ m s⁻¹, top view. (j) $V_F = 4.0$ m s⁻¹, front. (k) $V_F = 4.0$ m s⁻¹, lateral view. (l) $V_F = 4.0$ m s⁻¹, top view. (m) $V_F = 5.0$ m s⁻¹, front view. (n) $V_F = 5.0$ m s⁻¹, lateral view. (o) $V_F = 5.0$ m s⁻¹, top view.

As shown in Fig. 12b, e, h, k, and n, when the flight speed of drone (2.0 m s⁻¹) was constant, the backward tilt of the wake was same at each flight altitude. However, as flight altitude increased, the airflow was further behind the drone before it reached the ground. Therefore, as flight altitude increases the more the location of spray deposition appears further behind the drone.

4.4. Velocity distribution on the horizontal detection surface

The vertical downward velocity (V_{-Y}) of the airflow plays a leading role in the delivery of the spray to the target, and that determines the depth of spray penetration into the crop canopy (Chen et al., 2017). If V_{-Y} is too large, crop lodging may

occur; but if V_{-Y} is too small penetration of the spray into the crop will be poor. Therefore, finding the appropriate values for V_{-Y} is important.

The velocity distribution on the horizontal detection surface with a vertical height of 1 m from the ground was analysed. The spacing between the sampling points on the detection surface in the X-direction was 0.01 m, and the spacing in the Z-direction was 0.1 m. In addition, V_{+Y} indicated that the velocity direction was vertically upward. The velocity distribution range on the detection surface can characterise the contact range between the airflow and the crop canopy, which is the range that the droplet can cover on a horizontal surface. The range size is measured by the equivalent area bounded by the velocity of 0.5 m s⁻¹ (Li et al., 2019). The calculation formula is as follows:

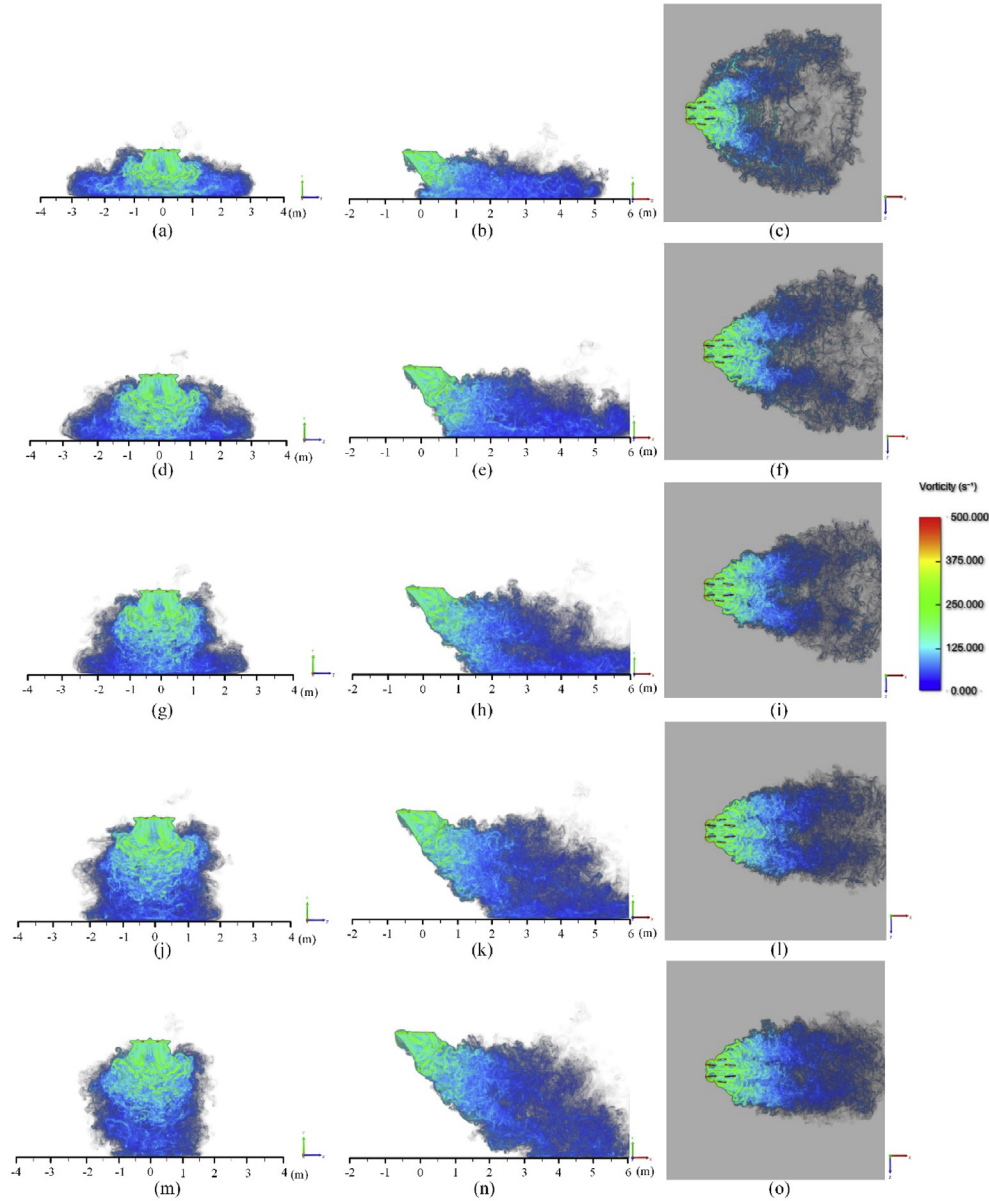


Fig. 12 – Vorticity distribution diagram at different flight altitudes ($V_F = 2.0 \text{ m s}^{-1}$, $t = 2.5 \text{ s}$). (a) $H_F = 1.5 \text{ m}$, front view. (b) $H_F = 1.5 \text{ m}$, lateral view. (c) $H_F = 1.5 \text{ m}$, top view. (d) $H_F = 2.0 \text{ m}$, front view. (e) $H_F = 2.0 \text{ m}$, lateral view. (f) $H_F = 2.0 \text{ m}$, top view. (g) $H_F = 2.5 \text{ m}$, front view. (h) $H_F = 2.5 \text{ m}$, lateral view. (i) $H_F = 2.5 \text{ m}$, top view. (j) $H_F = 3.0 \text{ m}$, front view. (k) $H_F = 3.0 \text{ m}$, lateral view. (l) $H_F = 3.0 \text{ m}$, top view. (m) $H_F = 3.5 \text{ m}$, front view. (n) $H_F = 3.5 \text{ m}$, lateral view. (o) $H_F = 3.5 \text{ m}$, top view.

$$S = S_0 \times \frac{n}{N} \% \quad (13)$$

where S is the airflow coverage equivalent area, m^2 ; S_0 is the area of the detection surface, m^2 ; n is the number of sampling points where V_{-Y} is not less than 0.5 m s^{-1} on the detection surface; N is the total number of V_Y (V_{-Y} and V_{+Y}) sampling points on the detection surface.

The 3D colormap surface with projection of V_Y was drawn using Origin software (OriginLab, Massachusetts, USA). A positive value of V_Y indicated that the velocity direction was consistent with V_{-Y} ; a negative value of V_Y indicated that the velocity direction was consistent with V_{+Y} . Figure 13 shows the distribution of V_Y on the detection surface when the drone

in hovering at $H_F = 3.0 \text{ m}$ and $t = 2.5 \text{ s}$. For easy observation, the transparency of the upper projection map was adjusted to 60%. The peak value of V_{-Y} on the detection surface appeared in the central area, reaching a peak of 8.4 m s^{-1} ; the reverse airflow at the edge caused a peak value of V_{+Y} of 1.3 m s^{-1} ; the airflow coverage equivalent area was 2.4 m^2 , which was distributed directly below the drone (Fig. 13).

Li et al. (2015) found that a “steep” effect exists in the distribution shape of airflow field in the direction of flight (Fig. 14h). As shown in Fig. 14h, the rate of increase of the airflow velocity at the front of the wake is significantly higher than the rate of decrease of the airflow velocity towards the rear. This meant that the airflow velocity at a location within the wake had a rapid rise and then a gentle fall. Similarly, the

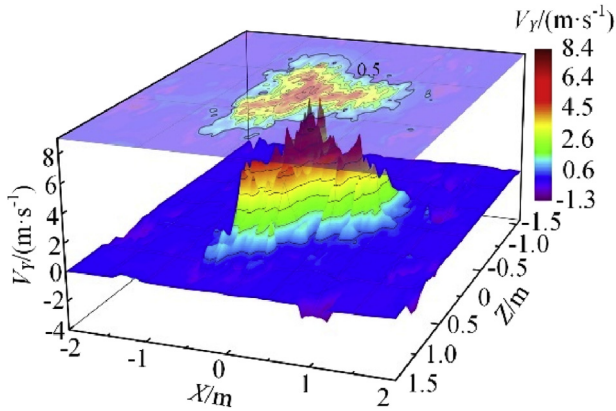


Fig. 13 – 3D colormap surface with projection of V_Y in hovering ($H_F = 3.0$ m, $t = 2.5$ s).

peak V_Y values all appeared at the front of the equivalent area, and the velocity value also had a significant “steep” effect. As shown in Fig. 14, when the drone was flying forward, the airflow coverage area on the detection surface was no longer distributed directly below the drone but moved towards the rear of the drone with the increasing flight speed and altitude. When the flight altitude was constant at 3.0 m, for flight speeds of 1.0 m s^{-1} , 2.0 m s^{-1} and 3.0 m s^{-1} (Fig. 14a,b and c), the peak V_Y values were 7.3 m s^{-1} , 5.7 m s^{-1} and

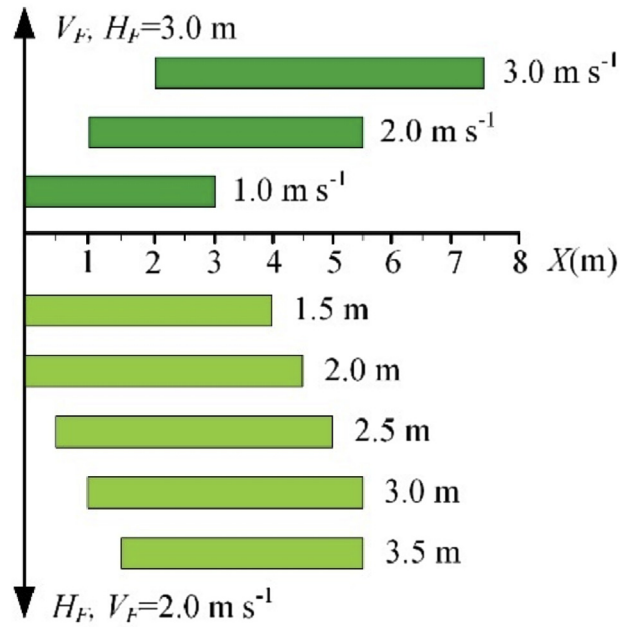


Fig. 15 – Schematic diagram of the position of the equivalent area in the X -direction.

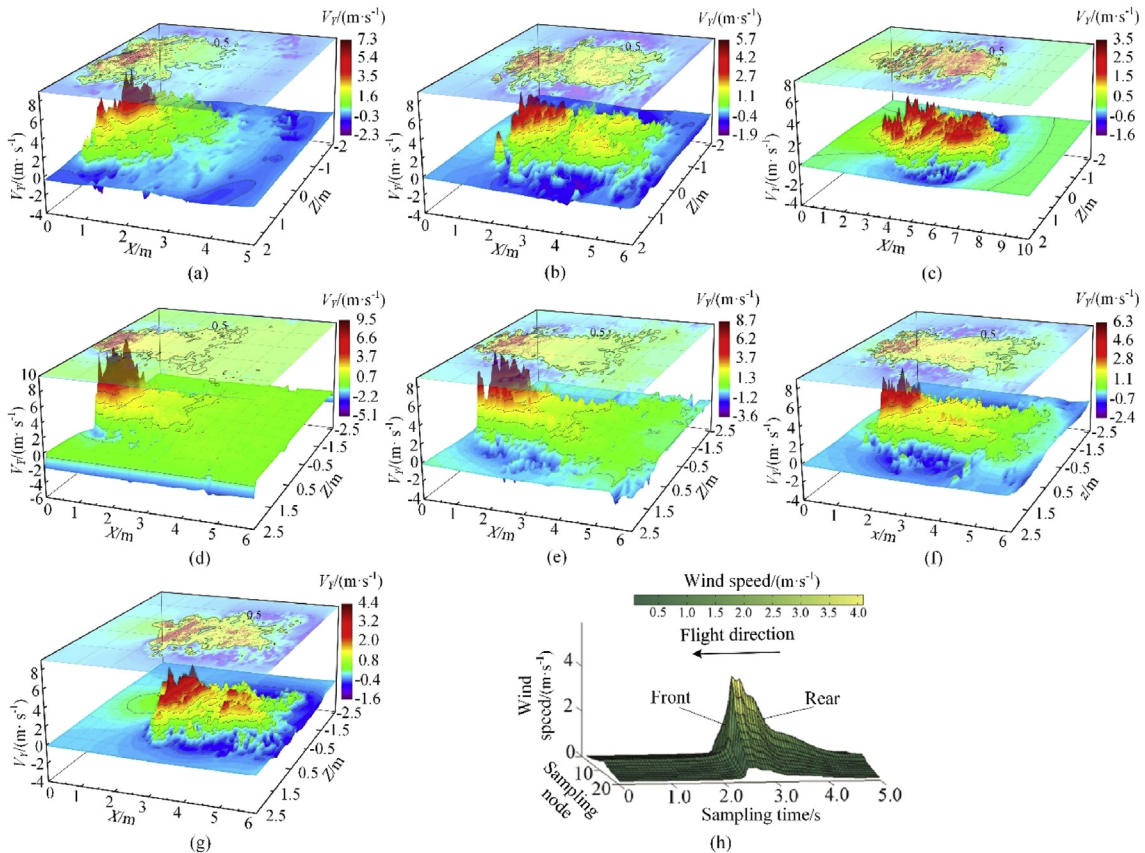


Fig. 14 – 3D colormap surface with projection of V_Y at different flight speeds and altitudes ($t = 2.5$ s). (a) $V_F = 1.0 \text{ m s}^{-1}$, $H_F = 3.0$ m. (b) $V_F = 2.0 \text{ m s}^{-1}$, $H_F = 3.0$ m. (c) $V_F = 3.0 \text{ m s}^{-1}$, $H_F = 3.0$ m. (d) $V_F = 2.0 \text{ m s}^{-1}$, $H_F = 1.5$ m. (e) $V_F = 2.0 \text{ m s}^{-1}$, $H_F = 2.0$ m. (f) $V_F = 2.0 \text{ m s}^{-1}$, $H_F = 2.5$ m. (g) $V_F = 2.0 \text{ m s}^{-1}$, $H_F = 3.5$ m. (h) “steep” effect from Li et al. (2015).

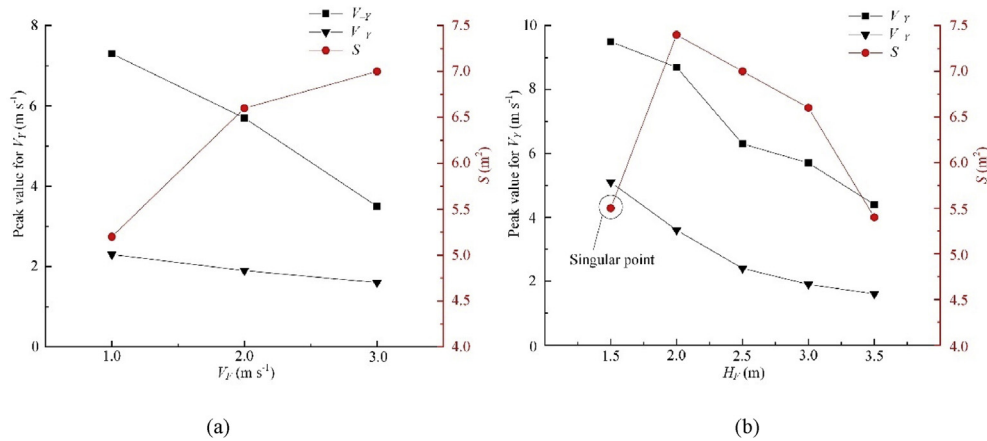


Fig. 16 – The effect of flight speeds and altitudes on peak values of V_Y and the equivalent area. (a) The effect of flight speed, $H_F = 3.0$ m. (b) The effect of flight altitude, $V_F = 2.0$ m s⁻¹.

3.5 m s⁻¹, respectively; the peak V_{+Y} values were 2.3 m s⁻¹ (for 1.0 m s⁻¹), 1.9 m s⁻¹ (for 2.0 m s⁻¹) and 1.6 m s⁻¹ (for 3.0 m s⁻¹) with equivalent areas of 5.2 m², 6.6 m² and 7.0 m². Moreover, the length of the equivalent area in X-direction increased from 3.0 m to 4.5 m when flight speed increased from 1.0 m s⁻¹ to 2.0 m s⁻¹. It then continued to increase from 4.5 m to 5.5 m as the flight speed increased from 2.0 m s⁻¹ to 3.0 m s⁻¹ (Fig. 15). When the flight speed was kept constant at 2.0 m s⁻¹ and the flight altitude was 1.5 m, 2.0 m, 2.5 m, 3.0 m and 3.5 m (Fig. 14d,e,f,b and g), the peak V_{-Y} values were 9.5 m s⁻¹, 8.7 m s⁻¹, 6.3 m s⁻¹, 5.7 m s⁻¹ and 4.4 m s⁻¹, respectively; the peak V_{+Y} values were 5.1 m s⁻¹ (for 1.5 m), 3.6 m s⁻¹ (for 2.0 m), 2.4 m s⁻¹ (for 2.5 m), 1.9 m s⁻¹ (for 3.0 m) and 1.6 m s⁻¹ (for 3.5 m) and the equivalent areas were 5.5 m², 7.4 m², 7.0 m², 6.6 m² and 5.4 m². Moreover, the distribution length of equivalent area in X-direction increased from 4.0 m to 4.5 m when flight altitude increased from 1.5 m to 2.0 m. It then remained at 4.5 m as the flight altitude continued to increase from 2.0 m to 2.5 m and 3.0 m but decreased from 4.5 m to 3.0 m when flight altitude increased from 3.0 m to 3.5 m (Fig. 15). Figure 15 also shows the position of the equivalent area in the X-direction.

In summary, for the flight parameters considered here, when the flight altitude was kept constant at $H_F = 3.0$ m, as the flight speed increased, the peak values for V_{-Y} and V_{+Y} decreased, and the equivalent area gradually increased (Fig. 16a). When the flight speed was kept constant at $V_F = 2.0$ m s⁻¹, as the flight altitude increased, the peak values for V_{-Y} and V_{+Y} decreased, and equivalent area also decreased except for the singular point (Fig. 16b). It was noted that when the flight altitude was 1.5 m, the peak V_{+Y} value was 5.1 m s⁻¹ with an equivalent area of 5.5 m². This can be attributed to the large reverse airflow velocity from the airflow spreading across the ground. As the flight speed or flight altitude increased, the V_{-Y} distribution within the equivalent area tended to be uniform. This implied that the “steep” effect had gradually weakened. Among them, when $V_F = 3.0$ m s⁻¹ and $H_F = 3.0$ m, the distribution of V_{-Y} was the most uniform (Fig. 14c). In addition, when the flight altitude was 1.5 m, the peak V_{-Y} value was 9.5 m s⁻¹, and the “steep” effect was the

most significant (Fig. 14d). Although it helps the droplets to penetrate into the crop canopy, large airflow velocity could cause lodging of cereal crops (such as wheat and rice). Therefore, this flight altitude should be avoided during spraying.

5. Conclusions and future work

A three-dimensional model of the airflow field of a six-rotor plant protection drone was developed using the LBM. The distribution characteristics of airflow field of the drone in hover and at varied flight speeds and altitudes were analysed. All field measurements were within 95% prediction interval of the Y-DAVA model, indicating that the airflow field was simulated successfully by LBM. During the pesticide application process, a reasonable flight speed and altitude should be sought between ensuring application efficiency, reducing drift, increasing the penetration of droplets in crop canopy and avoiding crop lodging. All the results of cases presented so far, based on simulation data, point to the fact that the flight speed and altitude can significantly affect the distribution characteristics of airflow field. When the flight speed was 4.0 m s⁻¹ and 5.0 m s⁻¹, the wake of the airflow field lifted off the ground, and transverse separation appeared as horseshoe vortices. Thus, operating parameters of $V_F = 4.0$ m s⁻¹ and 5.0 m s⁻¹ or $H_F = 1.5$ m should be avoided for pesticide spraying. When the flight altitude was constant ($H_F = 3.0$ m), as the flight speed increased, the peak values of V_{-Y} and V_{+Y} decreased, and the equivalent area increased. When the flight speed was constant ($V_F = 2.0$ m s⁻¹), as the flight altitude increased, the peak values of V_{-Y} and V_{+Y} decreased, and equivalent area also decreased. In addition, when $V_F = 3.0$ m s⁻¹ and $H_F = 3.0$ m, the distribution of V_{-Y} was almost homogenous. Wind conditions and crop canopy types are also important influencing factors and future work should take into consideration these and other influencing factors (including droplet size, wind conditions, and canopy interaction) to construct a model for precision spraying using six-rotor drones.

Declaration of Competing Interest

The authors declare that they have no known competing financial interests or personal relationships that could have appeared to influence the work reported in this paper.

Acknowledgements

This work was supported by the National Key Research and Development Plan of China (2017YFD0701400 and 2016YFD0200700).

REFERENCES

- Aidun, C. K., & Clausen, J. R. (2010). Lattice-Boltzmann method for complex flows. *Annual Review of Fluid Mechanics*, 42, 439–472. <https://doi.org/10.1146/annurev-fluid-121108-145519>
- Akesson, N. B., & Yates, W. E. (1974). *The use of aircraft in agriculture* (1rd ed.). Italy: FAO Press (Chapter 1).
- Bauknecht, A., Ewers, B., Schneider, O., & Raffel, M. (2017). Blade tip vortex measurements on actively twisted rotor blades. *Experiments in Fluids*, 58(5), 49. <https://doi.org/10.1007/s00348-017-2312-3>
- Bhamjee, M., Connell, S. H., & Nel, A. L. (2014). An investigation into the applicability of the lattice Boltzmann method to modelling of the flow in a hydrocyclone. In 9th South African Conference on Computational and Applied Mechanics, Somerset West. <http://hdl.handle.net/10210/11434>.
- Bludau, J., Rauleder, J., Friedmann, L., & Hajek, M. (2017). Real-time simulation of dynamic inflow using rotorcraft flight dynamics coupled with a lattice-Boltzmann based fluid simulation. In AIAA SciTech Forum-55th AIAA Aerospace Sciences Meeting, AIAA 2017–0050. <https://doi.org/10.2514/6.2017-0050>
- Chen, S., & Doolen, G. D. (1998). Lattice Boltzmann method for fluid flows. *Annual Review of Fluid Mechanics*, 30, 329–364. <https://doi.org/10.1146/annurev.fluid.30.1.329>
- Chen, S., Lan, Y., Bradley, K. F., Li, J., Liu, A., & Mao, Y. (2017). Effect of wind field below rotor on distribution of aerial spraying droplet deposition by using multi-rotor UAV. *Transactions of the Chinese Society for Agricultural Machinery*, 48(8), 105–113. <https://doi.org/10.6041/j.issn.1000-1298.2017.08.011>
- Chen, S., Wang, Z., Shan, X., & Doolen, G. D. (1992). Lattice Boltzmann computational fluid dynamics in three dimensions. *Journal of Statistical Physics*, 68(3–4), 379–400. <https://doi.org/10.1007/BF01341754>
- Ferziger, J. H., & Perić, M. (2002). *Computational methods for fluid dynamics* (3rd ed.). Germany: Springer-Verlag Berlin Heidelberg 2002 (Chapter 7).
- Giles, D. K., Akesson, N. B., & Yates, W. E. (2008). Pesticide application technology research and development and the growth of the industry. *Transactions of the ASABE*, 51(2), 397–403. <https://doi.org/10.13031/2013.24377>
- Gourdain, N., Jardin, T., Serre, R., Prothin, S., & Moschetta, J. M. (2018). Application of a lattice Boltzmann method to some challenges related to micro-air vehicles. *International Journal of Micro Air Vehicles*, 10(3), 285–299. <https://doi.org/10.1177/1756829318794174>
- Guo, Z., & Zheng, C. (2008). *Theory and applications of Lattice Boltzmann method*. Beijing, China: Science Press (Chapter 1).
- Guo, Q., Zhu, Y., Tang, Y., Hou, C., He, Y. Z., et al. (2020). CFD simulation and experimental verification of the spatial and temporal distributions of the downwash airflow of a quad-rotor agricultural UAV in hover. *Computers and Electronics in Agriculture*, 172, 105343. <https://doi.org/10.1016/j.compag.2020.105343>
- He, X., Bonds, J., Herbst, A., & Langenakens, J. (2017). Recent development of unmanned aerial vehicle for plant protection in east Asia. *International Journal of Agricultural and Biological Engineering*, 10(3), 18–30. <https://doi.org/10.3965/j.ijabe.20171003.3248>
- Hong, S., Zhao, L., & Zhu, H. (2018). CFD simulation of airflow inside tree canopies discharged from air-assisted sprayers. *Computers and Electronics in Agriculture*, 149, 121–132. <https://doi.org/10.1016/j.compag.2017.07.011>
- Janssen, C., & Krafczyk, M. (2010). A lattice Boltzmann approach for free-surface-flow simulations on non-uniform block-structured grids. *Computers and Mathematics with Applications*, 59(7), 2215–2235. <https://doi.org/10.1016/j.camwa.2009.08.064>
- Jorge, M., Pablo, A., Juan, A., & Manuel, P. (2020). Spray and economics assessment of a UAV-based ultra-low-volume application in olive and citrus orchards. *Precision Agriculture*, 21, 226–243. <https://doi.org/10.1007/s11119-019-09665-7>
- Lan, Y., Chen, S., & Fritz, B. K. (2017). Current status and future trends of precision agricultural aviation technologies. *International Journal of Agricultural and Biological Engineering*, 10(3), 1–17. <https://doi.org/10.3965/j.ijabe.20171003.3088>
- Li, J., Lan, Y., & Shi, Y. (2018). Research progress on airflow characteristics and field pesticide application system of rotary-wing UAV. *Transactions of the Chinese Society of Agricultural Engineering*, 34(12), 104–118. <https://doi.org/10.3969/j.issn.1002-6819.2018.12.013>
- Li, J., Shi, Y., Lan, Y., & Guo, S. (2019). Vertical distribution and vortex structure of rotor wind field under the influence of rice canopy. *Computers and Electronics in Agriculture*, 159, 140–146. <https://doi.org/10.1016/j.compag.2019.02.027>
- Li, J., Zhou, Z., Hu, L., Zang, Y., Xu, S., et al. (2014). Optimization of operation parameters for supplementary pollination in hybrid rice breeding using round multi-axis multi-rotor electric unmanned helicopter. *Transactions of the Chinese Society of Agricultural Engineering*, 30(11), 1–9. <https://doi.org/10.3969/j.issn.1002-6819.2014.11.001>
- Li, J., Zhou, Z., Lan, Y., Hu, L., Zang, Y., et al. (2015). Distribution of canopy wind field produced by rotor unmanned aerial vehicle pollination operation. *Transactions of the Chinese Society of Agricultural Engineering*, 31(3), 77–86. <https://doi.org/10.3969/j.issn.1002-6819.2015.03.011>
- Malaspinas, O., & Sagaut, P. (2014). Wall model for large-eddy simulation based on the lattice Boltzmann method. *Journal of Computational Physics*, 275, 25–40. <https://doi.org/10.1016/j.jcp.2014.06.020>
- Men, Y., Lai, Y., Dong, S., Du, X., & Liu, Y. (2017). Research on CO dispersion of a vehicular exhaust plume using lattice Boltzmann method and large eddy simulation. *Transportation Research Part D: Transport and Environment*, 52, 202–214. <https://doi.org/10.1016/j.trd.2017.03.012>
- Premnath, K. N., & Banerjee, S. (2011). On the three-dimensional central moment lattice Boltzmann method. *Journal of Statistical Physics*, 143(4), 747–794. <https://doi.org/10.1007/s10955-011-0208-9>
- Qiu, L., Tian, L., Liu, X., & Han, Y. (2019). A 3D multiple-relaxation-time LBM for modeling landslide-induced tsunami waves. *Engineering Analysis with Boundary Elements*, 102, 51–59. <https://doi.org/10.1016/j.enganabound.2019.02.011>
- Sjöholm, M., Angelou, N., Hansen, P., Hansen, K. H., Mikkelsen, T., et al. (2014). Two-dimensional rotorcraft downwash flow field measurements by lidar-based wind scanners with agile beam steering. *Journal of Atmospheric and Oceanic Technology*, 31(4), 930–937. <https://doi.org/10.1175/JTECH-D-13-00010.1>

- Tang, Y., Hou, C. J., Luo, S. M., Lin, J. T., Yang, Z., & Huang, W. F. (2018). Effects of operation height and tree shape on droplet deposition in citrus trees using an unmanned aerial vehicle. *Computers and Electronics in Agriculture*, 148, 1–7. <https://doi.org/10.1016/j.compag.2018.02.026>
- Wall, B. G., & Richard, H. (2006). Analysis methodology for 3C-PIV data of rotary wing vortices. *Experiments in Fluids*, 40(5), 798–812. <https://doi.org/10.1007/s00348-006-0117-x>
- Wang, P., Hu, L., Zhou, Z., Yang, W., Liu, A., et al. (2013). Wind field measurement for supplementary pollination in hybrid rice breeding using unmanned gasoline engine single-rotor helicopter. *Transactions of the Chinese Society of Agricultural Engineering*, 29(3), 54–61. <https://doi.org/10.3969/j.issn.1002-6819.2013.03.008>
- Weickert, M., Teike, G., Schmidt, O., & Sommerfeld, M. (2010). Investigation of the LES WALE turbulence model within the lattice Boltzmann framework. *Computers and Mathematics with Applications*, 59(7), 2200–2214. <https://doi.org/10.1016/j.camwa.2009.08.060>
- Wen, S., Han, J., Lan, Y., Yin, X., & Lu, Y. (2018). Influence of wing tip vortex on drift of single rotor plant protection unmanned aerial vehicle. *Transactions of the Chinese Society for Agricultural Machinery*, 49(8), 127–137+160. <https://doi.org/10.6041/j.issn.1000-1298.2018.08.015>
- Wen, S., Han, J., Ning, Z., Lan, Y., Yin, X., et al. (2019). Numerical analysis and validation of spray distributions disturbed by quad-rotor drone wake at different flight speeds. *Computers and Electronics in Agriculture*, 166, 105036. <https://doi.org/10.1016/j.compag.2019.105036>
- Yang, F., Xue, X., Cai, C., & Zhou, Q. (2018a). Effect of down wash airflow in hover on droplet motion law for multi-rotor unmanned plant protection machine. *Transactions of the Chinese Society of Agricultural Engineering*, 34(2), 64–73. <https://doi.org/10.11975/j.issn.1002-6819.2018.02.009>
- Yang, F., Xue, X., Zhang, L., & Sun, Z. (2017). Numerical simulation and experimental verification on downwash air flow of six-rotor agricultural unmanned aerial vehicle in hover. *International Journal of Agricultural and Biological Engineering*, 10(4), 41–53. <https://doi.org/10.25165/j.ijabe.20171004.3077>
- Yang, S., Yang, X., & Mo, J. (2018b). The application of unmanned aircraft systems to plant protection in China. *Precision Agriculture*, 19, 278–292. <https://doi.org/10.1007/s11119-017-9516-7>
- Zhang, P., Deng, L., Lyu, Q., He, S., Yi, S., et al. (2016a). Effects of citrus tree-shape and spraying height of small unmanned aerial vehicle on droplet distribution. *International Journal of Agricultural and Biological Engineering*, 9(4), 45–52. <https://doi.org/10.3965/j.ijabe.20160904.2178>
- Zhang, D., Lan, Y., Chen, L., Wang, X., & Liang, D. (2014). Current status and future trends of agricultural aerial spraying technology in China. *Transactions of the Chinese Society for Agricultural Machinery*, 45(10), 53–59. <https://doi.org/10.6041/j.issn.1000-1298.2014.10.009>
- Zhang, H., Qi, L., Wu, Y., Liu, W., Cheng, Z., & Musiu, E. (2019). Spatio-temporal distribution of down-wash airflow for multi-rotor plant protection UAV based on porous model. *Transactions of the Chinese Society for Agricultural Machinery*, 50(2), 112–122. <https://doi.org/10.6041/j.issn.1000-1298.2019.02.012>
- Zhang, B., Tang, Q., Chen, L. ping, & Xu, M. (2016b). Numerical simulation of wake vortices of crop spraying aircraft close to the ground. *Biosystems Engineering*, 145, 52–64. <https://doi.org/10.1016/j.biosystemseng.2016.02.014>
- Zhang, S., Xue, X., Qin, W., Sun, Z., Ding, S., & Zhou, L. (2015). Simulation and experimental verification of aerial spraying drift on N-3 unmanned spraying helicopter. *Transactions of the Chinese Society of Agricultural Engineering*, 31(3), 87–93. <https://doi.org/10.3969/j.issn.1002-6819.2015.03.012>
- Zhang, S., Xue, X., Sun, Z., Zhou, L., & Jin, Y. (2017). Downwash distribution of single-rotor unmanned agricultural helicopter on hovering state. *International Journal of Agricultural and Biological Engineering*, 10(5), 14–24. <https://doi.org/10.25165/j.ijabe.20171005.3079>
- Zhou, Z., Ming, R., Zang, Y., He, X., Luo, X., & Lan, Y. (2017). Development status and countermeasures of agricultural aviation in China. *Transactions of the Chinese Society of Agricultural Engineering*, 33(20), 1–13. <https://doi.org/10.11975/j.issn.1002-6819.2017.20.001>